V European Conference on Computational Fluid Dynamics
ECCOMAS CFD 2010
J. C. F. Pereira and A. Sequeira (Eds)
Lisbon, Portugal,14-17 June 2010

ASSESSMENT OF SEVERAL TURBULENCE MODELS IN A SUPERSONIC CAR

G. Araya*, B. Evans, O. Hassan and K. Morgan

Civil & Computational Engineering Centre, Swansea University, Swansea SA2 8PP, UK.
*e-mail: araya@mailaps.org

Key words: RANS, turbulence models, compressible flow, supersonic

Abstract. *One of the key factors in simulating realistic wall–bounded flows at high Reynolds numbers is the selection of an appropriate turbulence model for the steady RANS equations. In this investigation, several turbulence models are explored in steady, compressible, turbulent flows over a supersonic car, the "BLOODHOUND SSC" [1], at Mach numbers up to 1.1. Furthermore, three turbulent models are considered: the Spalart–Allmaras [2], the Wilcox $k-\omega$ [3] and the Menter SST [4]. The FLITE flow solver [5] developed at Swansea University is applied, which follows a finite volume approach with stabilization and discontinuity capturing. A numerical benchmarking of the different turbulent models is also performed on classical CFD cases, such as the transonic RAE 2822 airfoil and ONERA M6 wing. However, modelling the aerodynamics of a supersonic car is very challenging. This is due to the presence of highly–separated flow regions and shock waves; not to mention the numerical modelling of the rotating wheels and accounting for the car–floor interaction.*

1 INTRODUCTION

Wall-bounded turbulent flows at high Reynolds numbers are mainly characterized by a wide range of time and length scales (Pope [6]). The governing equations or full Navier-Stokes (NS) equations are generally solved in order to capture all time scales and eddies in the turbulent flow. This approach (Direct Numerical Simulation) is highly accurate and supplies extensive information; however, it demands a very refined mesh to properly capture the smallest scales (of the order of the Kolmogorov scales [7]). As a consequence, significant computational resources are usually required, which makes this approach (i.e., DNS) almost unsuitable for industrial applications. In Large Eddy Simulations (LES) the large scales or eddies are directly solved and the effects of the small scales are modeled; thus, the filtered Navier-Stokes equations with an additional sub-grid scale stress term are computed. An extensive review can be found in Meneveau and Katz [8]. Even the appearance of LES has not completely solved the low resolution required in a boundary layer flow; particularly, in the near-wall region. Furthermore, the use of an hybrid approach (RANS-LES) to overcome the low resolution needed in wall-bounded flows is an emerging and promising area [9]; nevertheless, there is still a lot of ground to cover for industrial use. Therefore, from a perspective of turbulent industrial flow simulations, the Reynolds Averaged NavierStokes (RANS) equations are usually solved. RANS equations are obtained by time averaging the full NS equations. These equations require a model or closure to compute the Reynolds stresses originated by the correlation of turbulent fluctuations. In fact, these Reynolds stresses come from the convective terms of the NS equations after applying the time-averaging process. The selection of an appropriate turbulence model is crucial to accurately represent important physical aspects of the flow, such as boundary layer separation and shock-boundary layer interaction (Catalano and Amato [10]). Catalano and Amato [10] tested five different turbulence models in 2-D and 3-D classical aerodynamic applications: Spalart Allmaras, the Myong and Kasagi $k-\varepsilon$, Wilcox $k-\omega$, Kok TNT, and Menter SST. They concluded that the Menter SST model exhibited the best balance between the physical capabilities and the numerical robustness for the transonic and high-lift flows explored.
In the present study, one-equation (Spalart–Allmaras) and two-equation (Wilcox $k-\omega$ and Menter SST) turbulence models are implemented and validated in the FLITE flow solver. Numerical results from typical aerodynamic cases in compressible flows are shown and discussed. Finally, some preliminary numerical predictions over the supersonic car, "BLOODHOUND SSC", are illustrated.

2 Governing Equations

The unsteady compressible Navier-Stokes equations in integral form on a 3-D Cartesian domain read as follows,

$$\int_{\Omega} \frac{\partial U_i}{\partial t} d\mathbf{x} + \int_{\partial\Omega} F_{ij} n_j d\mathbf{x} = \int_{\partial\Omega} G_{ij} n_j d\mathbf{x}, \tag{1}$$

where $\Omega \subset \Re^3$ with surface $\partial\Omega$, n_j is the unit normal vector to $\partial\Omega$. In addition, the unknown vector of conservative variables is expressed as,

$$\mathbf{U} = \begin{bmatrix} \rho \\ \rho u_i \\ \rho\epsilon \end{bmatrix} \tag{2}$$

Where ρ is the fluid density, u_i represents the i^{th} component of the velocity vector and ϵ is the specific total energy. Furthermore, the inviscid and viscous flux tensors are given by,

$$\mathbf{F}_j = \begin{bmatrix} \rho u_j \\ \rho u_i u_j \\ u_i(\rho\epsilon + p) \end{bmatrix} \tag{3}$$

$$\mathbf{G}_j = \begin{bmatrix} 0 \\ \tau_{ij} \\ u_k\tau_{kj} - q_j \end{bmatrix} \tag{4}$$

respectively, where i varies from 1 to 3. The deviatoric stress tensor, τ_{ij} is defined as,

$$\tau_{ij} = -\frac{2}{3}\mu\frac{\partial u_k}{\partial x_k}\delta_{ij} + \mu\left(\frac{\partial u_i}{\partial x_j} + \frac{\partial u_j}{\partial x_i}\right), \tag{5}$$

where μ is the dynamic viscosity, and $q_j = -k\partial T/\partial x_j$ is the heat flux. Here, k is the thermal conductivity and T is the absolute temperature. The following assumptions are considered: i) the viscosity varies with temperature according to Sutherlands's law; ii) the Prandtl number is constant and equal to 0.72; iii) the gas is calorically perfect; iv) the medium is continuous; and, v) body forces, buoyancy and heat transfer by radiation are neglected.

In order to obtain the compressible RANS equations, the unsteady equations 1 must be averaged in time. The idea is to time-average the governing equations to smooth the instantaneous turbulent fluctuations in the flow field, while still being able to capture time-dependency in the time scales of interest. Of course, this averaging procedure breaks down if the time scale of the physical phenomena of relevance is of similar time scale as that of the turbulence itself. However, in many engineering problems, the assumption is valid; particularly, for flows where a statistically averaged steady state solution is sought. Hence, for compressible flows, the Favre averaging procedure is mostly employed and it is density weighted. The reader is referred to Sørensen's thesis [11] for further details.

3 Turbulence Modelling in RANS

The Favre averaging procedure in time of eq. 1 generated an extra convective term. This term is referred to as the Favre-averaged Reynolds-stress tensor, denoted by:

$$\tau_{ij}^R = -\overline{\rho u_i'' u_j''}. \tag{6}$$

The most straightforward approach is to associate the unknown Reynolds stresses with the computed mean flow quantities by means of a turbulence model or closure. If the Boussinesq hypothesis is applied, this results in a linear relationship to the mean flow strain tensor through the eddy viscosity [3]:

$$\tau_{ij}^R = \mu_t \left(\frac{\partial U_i}{\partial x_j} + \frac{\partial U_j}{\partial x_i} - \frac{2}{3} \frac{\partial U_k}{\partial x_k} \delta_{ij} \right) - \frac{2}{3} \rho k \delta_{ij}. \tag{7}$$

Here, k is the turbulent kinetic energy. Furthermore, the eddy viscosity, μ_t, depends on the velocity and the length scale of the turbulent eddies, i.e. $\mu_t \sim k^{1/2}\ell$, being ℓ the turbulence length scale. In this investigation, one and two transport equation models are considered. The idea of these turbulence models is to solve partial differential equations that describe the transport of the eddy viscosity; as a consequence, nonlocal and history effects on μ_t are taken into account. Particularly, in the one-equation turbulence model of SpalartAllmaras [2], a combination of the turbulent scales, so called the viscosity-like variable, $\bar{\nu}$, is obtained by solving an empirical transport equation. On the other hand, the two-equation turbulence models are complete because two transport equations are solved for both turbulent scales. In particular, the $k-\omega$ turbulence models have significantly increased its popularity during the last decade due to its good performance in boundary layers flows subjected to adverse pressure gradients with eventual separation. Nevertheless, the original $k-\omega$ model developed by Wilcox [3] exhibits a freestream dependency of ω. On the contrary, the $k-\epsilon$ model generally does not show this freestream dependency of ω. Menter [4] combined the advantages of both models by means of blending functions that permits to switch from $k-\omega$ (close to the wall) to $k-\epsilon$ as approaching the edge of a boundary layer. A second improvement performed by Menter [4] was a modification to the eddy viscosity based on the idea of Johnson-King model, which establishes that the transport of the main turbulent shear stresses is crucial in the simulations of strong adverse pressure gradient flows. This new approach was called shear-stress transport model, well known as Menter SST.

4 Results and Discussion

The FLITE flow solver [5] for unstructured meshes and a finite-volume approach is used in the assessment of Spalart–Allmaras, Wilcox $k-\omega$ and Menter SST turbulence models. Classical aerodynamic cases such as the supersonic flat plate, transonic RAE 2822 airfoil and ONERA M6 wing are presented in this section, with a final discussion about the BLOODHOUND SSC's numerical predictions.

4.1 Supersonic flatplate

Although the flat plate shows a very simple geometry without a streamwise pressure gradient; it is very appropriate to evaluate the performance of any turbulence model due to the extensive experimental data and theoretical/empirical correlations available from

the literature. In this study, a supersonic flat plate at a freestream Mach number, M_∞, equal to 2 is computed. The Reynolds number, $Re_x = xU_\infty/\mu_\infty$, based on the streamwise x-coordinate is 1×10^7 per unit length. The flat plate is approximately 4 unit-length long with a prescribed isentropic condition for the thermal field. A symmetry condition was imposed on the lower boundary face located upstream of the leading edge. Downstream of the flat plate (where the no-slip condition is assumed for the velocity), a freestream condition is prescribed. Similarly, at inflow, outflow and top surfaces, freestream values are imposed. This is a 3-D case with a symmetry condition assumed in lateral faces. The spanwise length is approximately 0.8 unit-length wide; hence, the computational box is wide enough to eliminate any influence from the lateral faces on the flow statistics. Furthermore, numerical results shown here were taken from the vicinity of the central longitudinal plane, far from lateral surfaces. Additionally, the height of the computational domain is sufficient ($\sim$ 0.8 unit-length) to allow a natural streamwise developing of the turbulent boundary layer.

Figure 1 shows the streamwise variation of the skin friction coefficient, C_f, as a function of Re_x. Generally speaking, the corresponding values obtained by Spalart–Allmaras, Wilcox $k-\omega$ and Menter SST turbulence models depict an excellent agreement with theoretical correlations from White [12] and Schlichting [13]; particularly, by the end of the flat plate. However, the Menter SST model exhibits a shorter transition and the C_f profile quickly tends to realistic values downstream from the leading edge. The mean streamwise velocity along the boundary layer follows the 1/7 power law distribution, as seen in fig. 2(a), for $Re_x = 34 \times 10^7$. Nevertheless, the velocity profile computed from the Wilcox $k-\omega$ model depicts some deviation from the 1/7 power law at $y/\delta \sim 0.05$. The thermal boundary layer plays a crucial role in compressible wall-bounded flows; consequently, it is very important its validation. In other words, the coupled behavior of the velocity and thermal fields should be properly represented. In fig. 2(b), the computed temperature distributions, T/T_∞, as a function of the mean streamwise velocity, U/U_∞, are plotted at a streamwise station where $Re_x = 34 \times 10^7$. For comparison, the theoretical relation by Crocco-Busemann (see page 502 in White [12]) is also included. The Crocco-Busemann relation assumes a linear variation of the total enthalpy across the boundary layer in zero pressure gradient with a unitary turbulent Prandtl number. Furthermore, present thermal profiles show a good agreement with the Crocco-Busemann relation. It is worth mentioning that the Crocco-Busemann relation is a function of the local wall-temperature; therefore, a different theoretical profile is obtained for each turbulence model. Finally, iso-contours of the turbulent kinetic energy, $k^* = k/U_\infty^2$, are shown in fig. 3 from the Menter SST model. The starting and ending points of the flat plate are represented by cross-sectional cutting planes. It is appreciated the natural evolution of k^* in the direction of the flow. This term is mainly responsible for triggering turbulence in the flow.

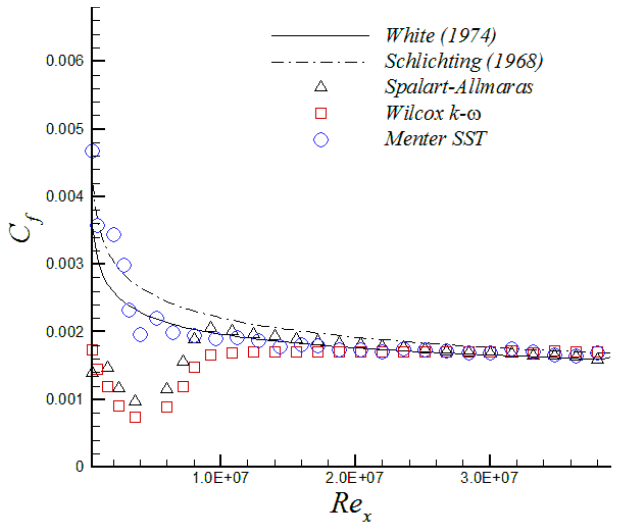

Figure 1: Skin friction coefficient as a function of Re_x.

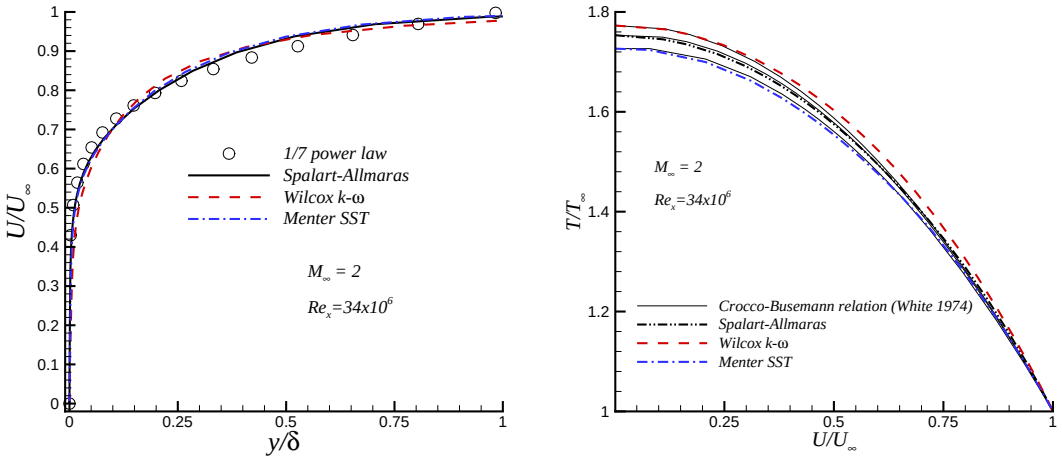

(a) (b)

Figure 2: Mean streamwise velocity (a) and temperature distribution (b) in the supersonic flat plate.

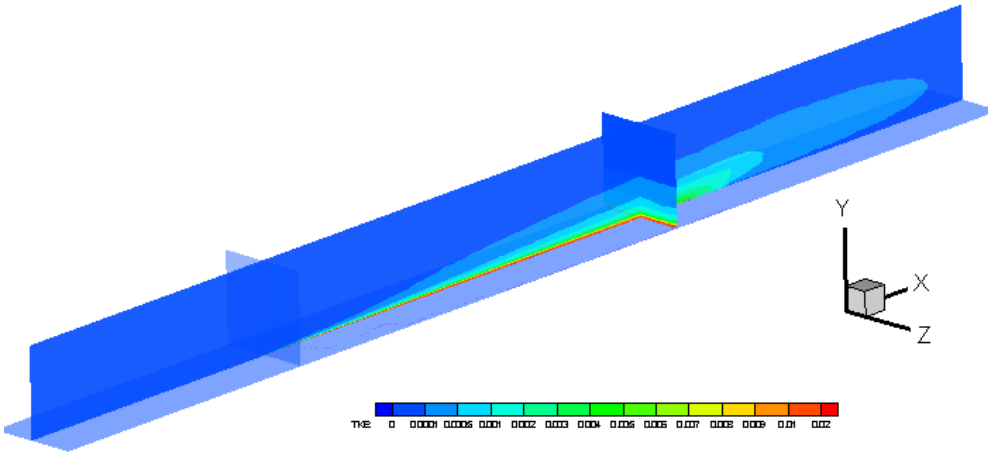

Figure 3: Iso-contours of turbulent kinetic energy in the supersonic flat plate (Menter SST).

4.2 Transonic RAE 2822 airfoil

The second example consists on the simulation of steady turbulent transonic flow around the RAE2822 airfoil. This is the standard test case 9 in [14] for turbulence models. The freestream Mach number, M_∞, is 0.73; the Reynolds number is 6.5×10^6 and the angle of attack is $\alpha = 2.79^o$. The mesh is 3-D and composed by tetrahedral. The initial mesh spacing in the normal direction at the surface is 1.0×10^{-6} or approximately $y^+ = 0.2$ in wall units.

Table 1 shows the computed values of lift, drag and momentum coefficients for the Spalart–Allmaras, Wilcox $k-\omega$ and Menter SST turbulence models as well as experimental data from the AGARD AR138 report [14]. For this mesh configuration, the Wilcox $k-\omega$ turbulence model has produced the best approximation on the lift coefficient (the error is approximately 3%). However, the Menter SST model possesses the best performance on drag calculations: 11 drag-counts of difference with the experimental value for the total drag, $C_{D\ total}$, and only 3 drag-counts for the friction drag, $C_{D\ friction}$. Furthermore, the errors computed on the moment coefficient at 25% of the chord were very similar for the Wilcox $k-\omega$ and Menter SST models ($\sim 8\%$). The pressure (C_p) and skin friction (C_f) coefficients are depicted by fig. 4 together with the corresponding experimental data. The C_p distribution of all turbulence models in 4(a) exhibits a peak close o the leading edge in the upper surface, not catched by experiments. It is the authors' understanding that this is due to physical aspects; however, it may be attributed to an insufficient mesh resolution in this zone and further exploration needs to be carried out. The Wilcox $k-\omega$ model produced the best prediction of the shock location and pressure recovery behind the shock in the upper surface, while the Spalart–Allmaras predicted a shock location more upstream. Furthermore, the numerical predictions of C_p in the lower surface almost overlap the experimental values in the three turbulence models. With respect to the C_f

Table 1: Lift, drag and moment coefficients in RAE2822

	Spalart-Allmaras	Wilcox $k-\omega$	Menter SST	Experiment
C_L	0.696	0.779	0.743	0.803
$C_{D\ total}$	0.0134	0.0154	0.0157	0.0168
$C_{D\ friction}$	0.0040	0.0042	0.0053	0.0050
$C_{m\ 25\%}$	-0.0913	-0.1066	-0.0998	-0.099

distribution, the Wilcox $k-\omega$ model was the only turbulence model that predicted a shock induced separation with a very small zone of separated flow at the upper part (see fig. 4(b)). In addition, the Menter SST model captured more appropriately the abrupt change in C_f at the shock location. However, the Menter SST model overpredicted the C_f values upstream of the shock location, where the Spalart–Allmaras and Wilcox $k-\omega$ turbulence models yielded more accurate results. On the other hand, all models underpredicted the skin friction in the lower surface, the Menter SST model gave a closer prediction to the only experimental value measured in the standard test case 9 in [14], as observed in fig. 4(b). In figure 5, the velocity profiles at $x/c = 0.404$, where the flow is attached, are depicted; and, all the numerical results are in excellent agreement with the experimental data. Figure 6 shows iso-contours of the mean streamwise velocity for the Wilcox $k-\omega$ model where it can be appreciated the location of the shock at $x/c \sim 0.55$.

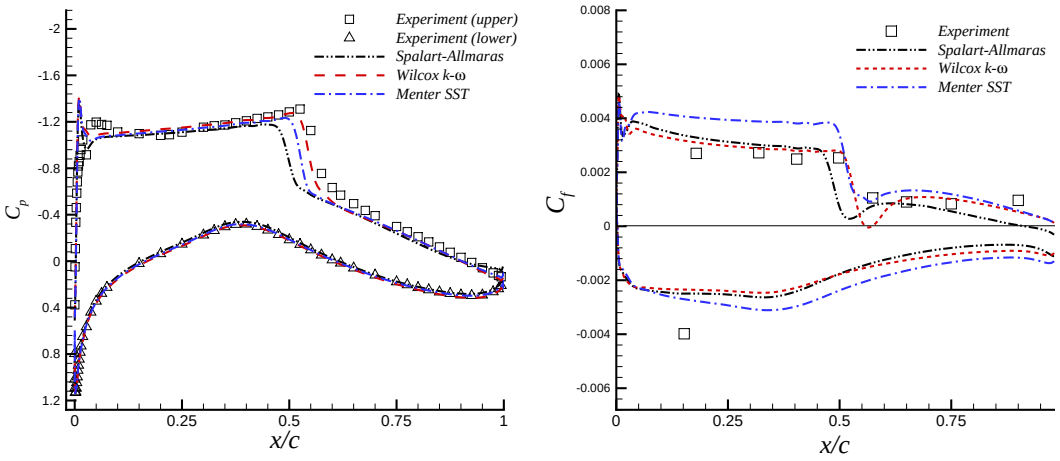

(a) (b)

Figure 4: Pressure coefficient (a) and skin friction (b) in the RAE2822 airfoil.

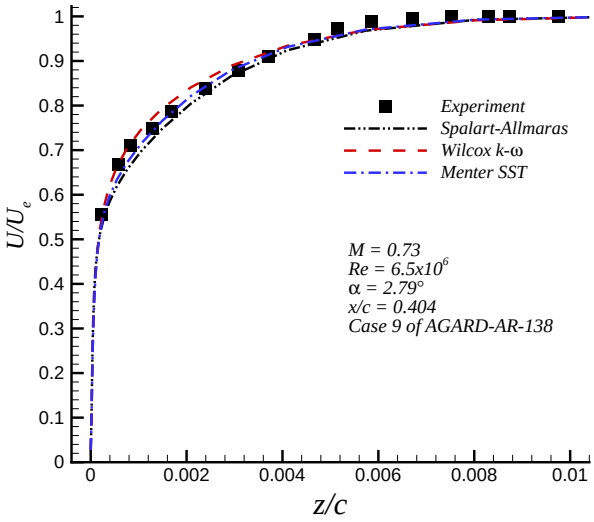

Figure 5: Mean streamwise velocity distribution at $x/c = 0.404$.

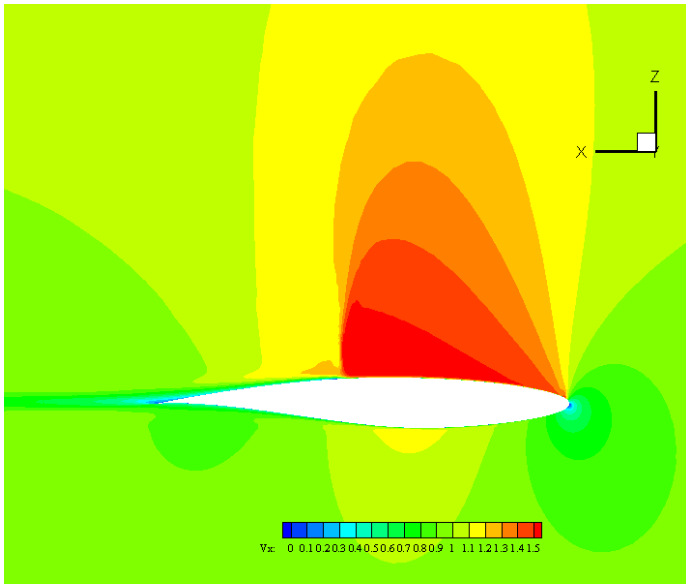

Figure 6: Iso-contours of mean streamwise velocity (Wilcox $k - \omega$).

4.3 ONERA M6 Wing

In this section, numerical results by the turbulence models are presented for the ONERA M6 wing [15]. The freestream Mach number, M_∞, is 0.84 and the total Reynolds number is 12×10^6 based on the mean geometric chord. This case is tested at two different angles of attack: $\alpha = 3.06^o$ and $\alpha = 6.0^o$. The latter represents a very challenging one for turbulence model evaluation due to the presence of highly separated flow. The hybrid mesh configuration is as follows: 6273852 tetrahedral elements, 2441561 prisms and 11600 pyramids with 109558 triangles in the surface. The mesh is composed by 35 viscous layers for boundary layer capturing and the first off-wall point is approximately at $y^+ = 0.4$ in wall units, for points located in the vicinity of the leading edge where the skin friction is high.

Table 2 contains information about the calculated values of lift and drag for the Spalart–Allmaras, Wilcox $k-\omega$ and Menter SST turbulence models. Furthermore, the lowest lift coefficient was obtained by the Menter SST model; on the other hand, the total and friction coefficients were the highest computed by this model. The pressure coefficient profiles are depicted by figure 7. In general, the three models show similar C_p at the different spanwise sections. However, the Menter SST model predicts better the shock location at sections $y/(b/2) = 0.2$ and 0.44 in the upper surface; while a better shock capturing is performed by Spalart–Allmaras and Wilcox $k-\omega$ models at $y/(b/2) = 0.65$. The skin friction coefficients, C_f, are plotted in fig. 8 at spanwise stations $y/(b/2) = 0.9$ and 0.95. It is observed a good agreement in all turbulence models about the location of the flow separation point: $x/c \sim 0.25$ and 0.2 for $y/(b/2) = 0.9$ and 0.95, respectively. Nevertheless, the downstream recovery of C_f is quite different in all turbulence models. The Wilcox $k-\omega$ and Menter SST turbulence models predicted similar reattachment lengths, while Spalart–Allmaras produced the largest reattachment length. In addition, the Menter SST model induced higher values for the skin friction downstream of the reattachment point, which is consistent with the largest values of $C_{D\ friction}$ obtained in table 2. From figure 9, iso-surfaces of negative streamwise velocities are extracted; and, it is observed that the recirculating flow bubble predicted by the Spalart–Allmaras model is bigger than that of the Menter SST model.

Some preliminary results for the ONERA M6 wing at $\alpha = 6.0^o$ are depicted by fig. 10, where contours of the streamwise velocity can be appreciated at a spanwise section of $y/(b/2) = 0.9$ for the Spalart–Allmaras and Menter SST approaches. The velocity distribution looks quite different for both models, with a separation zone significantly much larger in the Spalart–Allmaras results. This can be confirmed from fig. 11, the Spalart–Allmaras model yields a stronger reverse flow provoked by the detached vortex. Moreover, the flow reattachment occurs closer to the trailing edge in case of Spalart–Allmaras predictions than for Menter SST simulations. The module of vorticity is shown by fig. 12(a) at $y/(b/2) = 0.9$ obtained by the Menter SST model. Two strong vortices are generated at this spanwise section, one in the vicinity of the leading edge (i.e., $x/c \sim 0.25$) and the

Table 2: Lift and drag coefficients in ONERA M6 wing at $\alpha = 3.06^o$

	Spalart-Allmaras	Wilcox $k-\omega$	Menter SST
C_L	0.2596	0.2623	0.2530
$C_{D\ total}$	0.0175	0.0179	0.0189
$C_{D\ friction}$	0.0048	0.0051	0.0057

other at the trailing edge. The complex vortical structures generated on the upper surface at such a high angle of attack ($\alpha = 6.0^o$) are observed in fig. 12(b). There, iso-surfaces of vorticity with a normalized value of 1 are extracted; and, the detached vortices at the trailing edge are clearly observed. In summary, the two equation turbulence models (Wilcox $k-\omega$ and Menter SST) have demonstrated similar performance at the high-lift condition (i.e., $\alpha = 6.0^o$) where separated flows play an important role ($C_L \approx 0.34$). On the other hand, the very low lift computed by the Spalart–Allmaras model at this condition is consistent with other concluding remarks from the literature about the limitations of this model in predicting highly-separated turbulent flows.

4.4 Supersonic Car

Preliminary numerical predictions over a supersonic car, the "BLOODHOUND SSC", are shown and discussed in this section. Two different freestream Mach numbers, M_∞, are considered: 0.85 and 1.1, respectively. The total Reynolds number is approximately 325×10^6 based on the streamwise length of the car ($\sim 13m$). The Spalart–Allmaras (SA) and Wilcox $k-\omega$ turbulence models are tested together with the JST [16] and HLLC [17] schemes for convective flux calculation. Table 3 depicts the corresponding aerodynamic forces at $M_\infty = 0.85$ (i.e., lift, total drag and friction drag) normalized by the freestream dynamic pressure, q, and the integration surface, S. In general, the Spalart–Allmaras and Wilcox $k-\omega$ models have produced similar global aerodynamic forces over the car for the same convective flux scheme. The HLLC scheme yields roughly higher values for the lift and total drag. The residual history of the density is shown by fig. 13 for the Spalart–Allmaras and Wilcox $k-\omega$ turbulence models by considering the JST scheme at $M_\infty = 0.85$ with a much faster rate of converge in the Wilcox $k-\omega$'s predictions. Figure 14 exhibits the pressure coefficient distributions, C_p, at a centreline plane of the car for the following combinations: JST-SA vs. HLLC-SA (top), JST-SA vs. JST-k-ω (middle) and HLLC-SA vs. HLLC-k-ω (bottom). Generally speaking, the most significant discrepancies in C_p have been obtained for the two convective flux schemes considered (i.e., JST and HLLC) at the same turbulence model, being the HLLC more dissipative. Some interesting conclusions can be drawn from the different C_p profiles. Upstream of the intake duct, two zones of favorable pressure gradients (FPG) can be observed: mild and strong. This provokes a significant acceleration of the flow; as a consequence, a sufficient quality of the airflow to he inlet duct is ensured for a maximum efficiency of the engine.

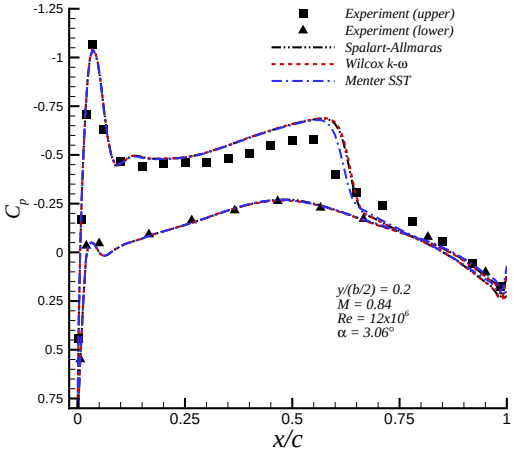

(a) $y/(b/2) = 0.2$

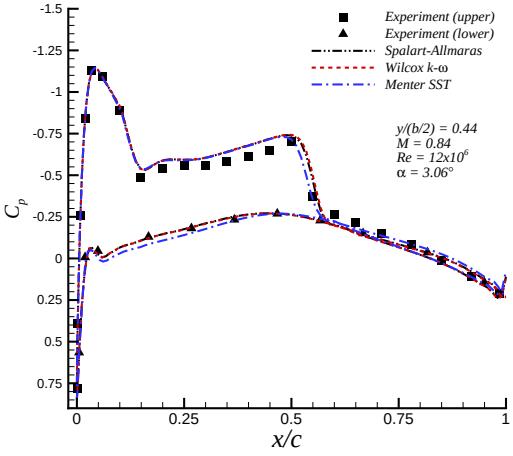

(b) $y/(b/2) = 0.44$

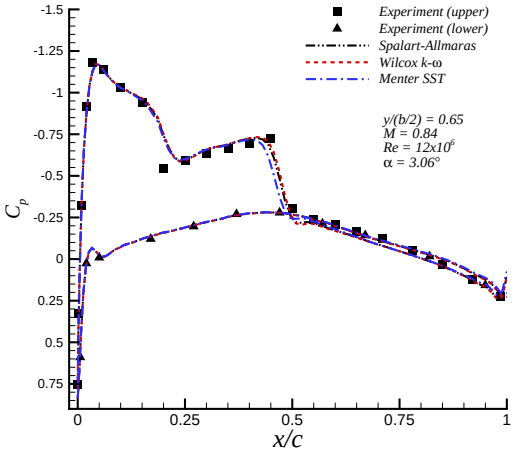

(c) $y/(b/2) = 0.65$

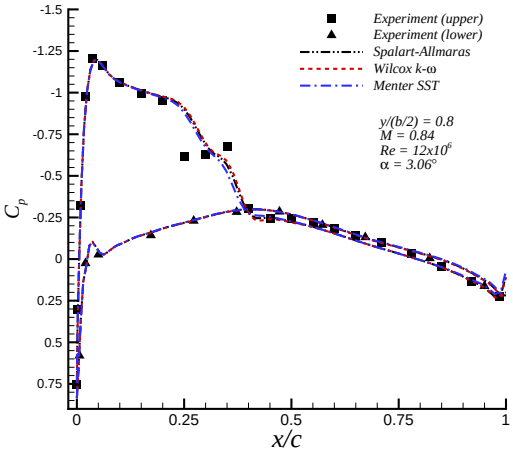

(d) $y/(b/2) = 0.8$

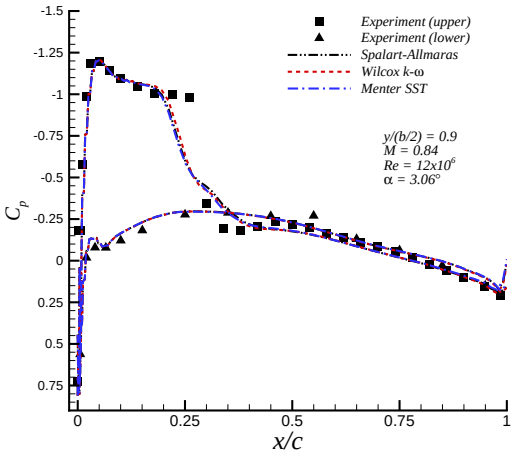

(e) $y/(b/2) = 0.9$

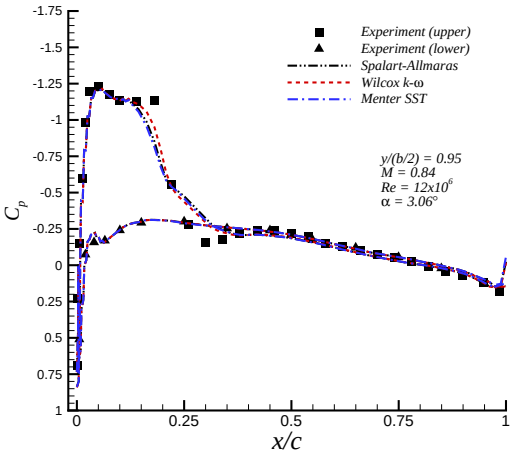

(f) $y/(b/2) = 0.95$

Figure 7: Pressure coefficient distributions in the ONERA M6 wing at $\alpha = 3.06^o$.

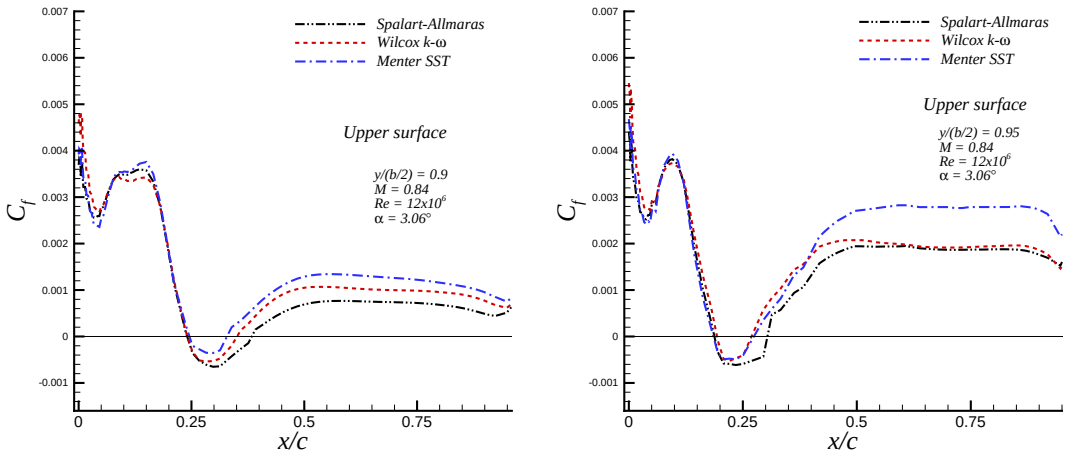

(a) $y/(b/2) = 0.9$ (b) $y/(b/2) = 0.95$

Figure 8: Skin friction distributions in the ONERA M6 wing at $\alpha = 3.06^o$.

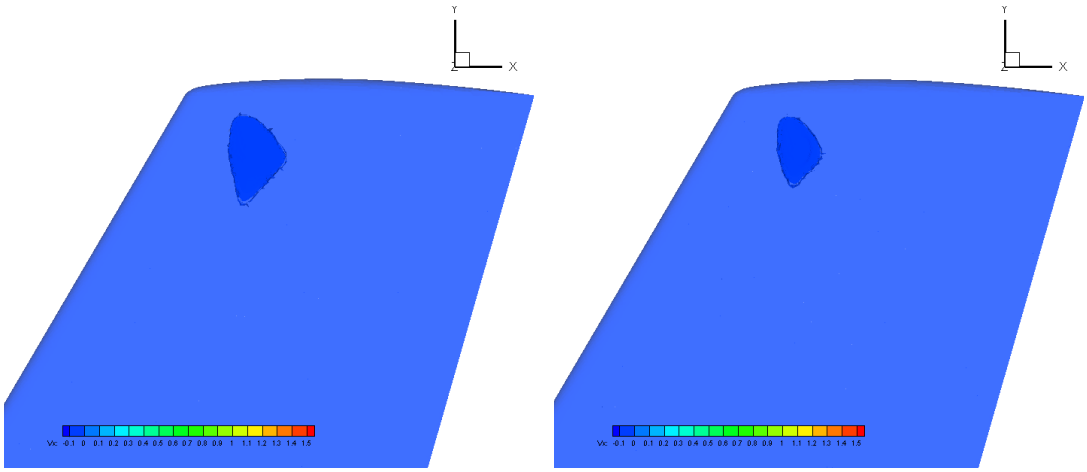

(a) Spalart-Allmaras (b) Menter SST

Figure 9: Iso-surfaces of streamwise velocity over the upper surface in the ONERA M6 wing at $\alpha = 3.06^o$.

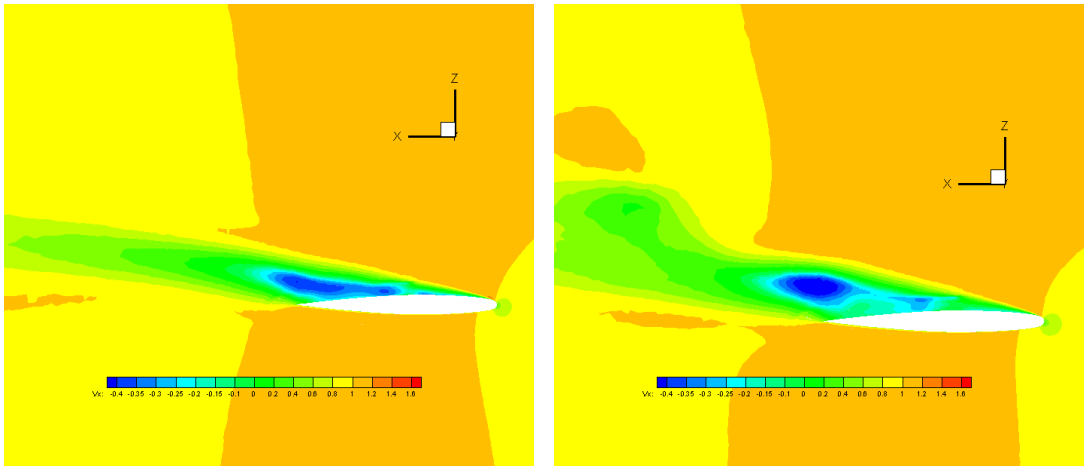

(a) Spalart-Allmaras (b) Menter SST

Figure 10: Iso-contours of streamwise velocity for $y/(b/2) = 0.9$ in the ONERA M6 wing at $\alpha = 6.0^o$.

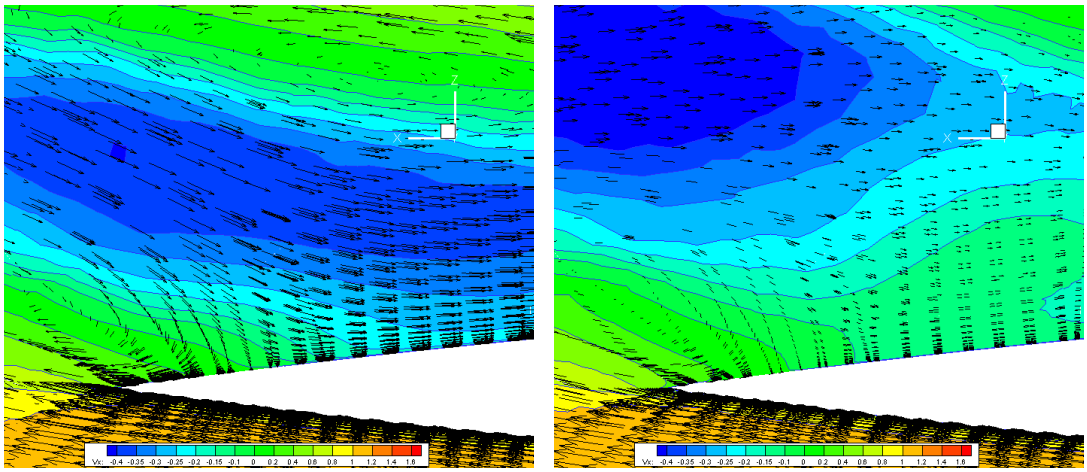

(a) Spalart-Allmaras (b) Menter SST

Figure 11: Zoom of velocity vectors for $y/(b/2) = 0.9$ in the ONERA M6 wing at $\alpha = 6.0^o$.

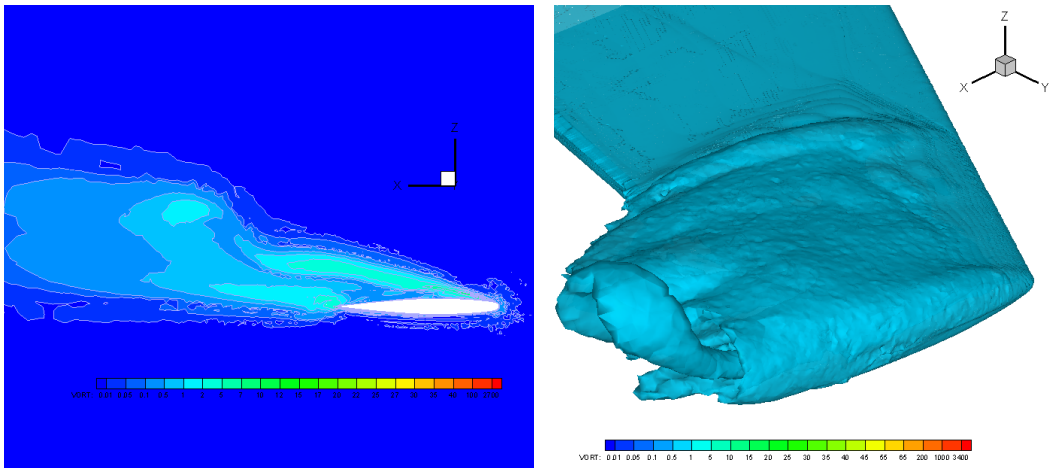

(a) Iso-contours of vorticity for $y/(b/2) = 0.9$ (b) Iso-surfaces of vorticity ($\bar{\omega} = 1$)

Figure 12: ONERA M6 wing at $\alpha = 6.0^o$ (Menter SST).

Downstream of the inlet duct, a zone of constant pressure gradient can be observed almost up to the vertical tail. Although a zero pressure gradient (ZPG) flow is not the best option to delay flow separation (an accelerating boundary layer or FPG flow has a better performance in delaying separation), it is not the worst case scenario because an adverse pressure pressure (APG) flow is more prone to boundary layer detachment.
Table 4 contains the lift and drag forces at a freestream Mach number of 1.1. In particular, the combination JST-k-ω blew up after some time steps (N/A) and ongoing investigations have been performed. The computed aerodynamic forces have been very consistent; perhaps, the greatest discrepancies ($\sim 40\%$) are observed in the friction drag for the combinations JST-SA vs. HLLC-k-ω. Figures 15 and 16 depict iso-contours of Mach numbers for $M_\infty = 0.85$ and 1.1, respectively. The longitudinal plane $(x-y)$ is located at $z = 0.5m$ from the floor and shows the rear part of the car. The blending approaches JST-SA vs. HLLC-SA are considered. Larger zones of low velocity (blue) behind the wheels and engine are predicted by JST-SA than those of HLLC-SA. These areas are more evident at lower freestream Mach numbers ($M_\infty = 0.85$), and, it can be related to vortex shedding processes. On the contrary, the HLLC-SA combination induces bigger zones of high Mach numbers in the car-wheel intersection. The outlet engine boundary condition provokes a free shear flow behind the car with low-velocity zones in the jet-atmosphere transition. Particularly, this zone of low Mach numbers is almost imperceptible in the HLLC-SA combination at $M_\infty = 1.1$ (see fig. 16(b)). Additionally, the decreasing cross-sectional shape of the car structure upstream of the engine induces an adverse pressure gradient zone (APG) with a decelerating boundary layer and eventual flow separation. This is confirmed by the zone of very low Mach numbers, which is more evident in the JST-SA scheme (fig. 16(a)).

Table 3: Aerodynamic forces over the BLOODHOUND SSC for $M_\infty = 0.85$

Spalart-Allmaras	$Lift/(q \times S)$	$TotalDrag/(q \times S)$	$FrictionDrag/(q \times S)$
JST	0.07	1.18	0.25
$HLLC$	0.25	1.45	0.10
Wilcox $k-\omega$	$Lift/(q \times S)$	$TotalDrag/(q \times S)$	$FrictionDrag/(q \times S)$
JST	0.10	1.18	0.24
$HLLC$	0.26	1.58	0.23

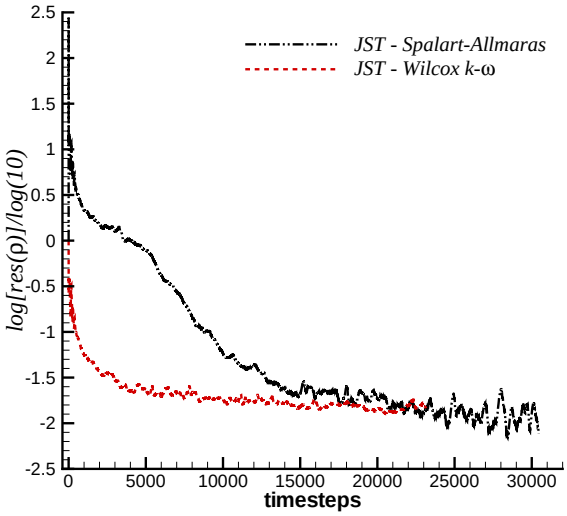

Figure 13: Residual history of density at $M_\infty = 0.85$

Table 4: Aerodynamic forces over the BLOODHOUND SSC for $M_\infty = 1.1$

Spalart-Allmaras	$Lift/(q \times S)$	$TotalDrag/(q \times S)$	$FrictionDrag/(q \times S)$
JST	0.42	1.61	0.06
$HLLC$	0.38	1.83	0.08
Wilcox $k-\omega$	$Lift/(q \times S)$	$TotalDrag/(q \times S)$	$FrictionDrag/(q \times S)$
JST	N/A	N/A	N/A
$HLLC$	0.40	1.84	0.10

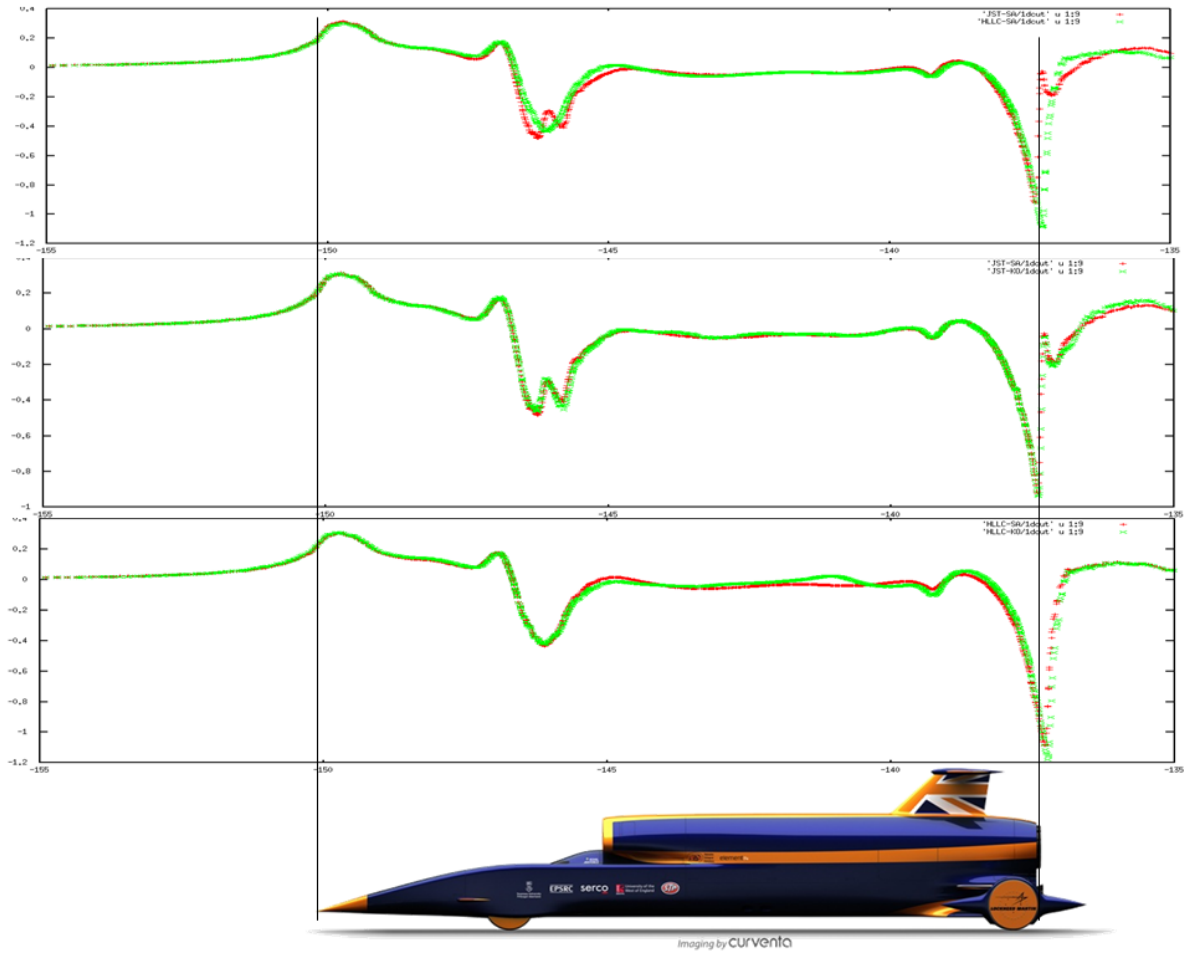

Figure 14: Pressure coefficient distributions, C_p in ground centreline at $M_\infty = 0.85$.

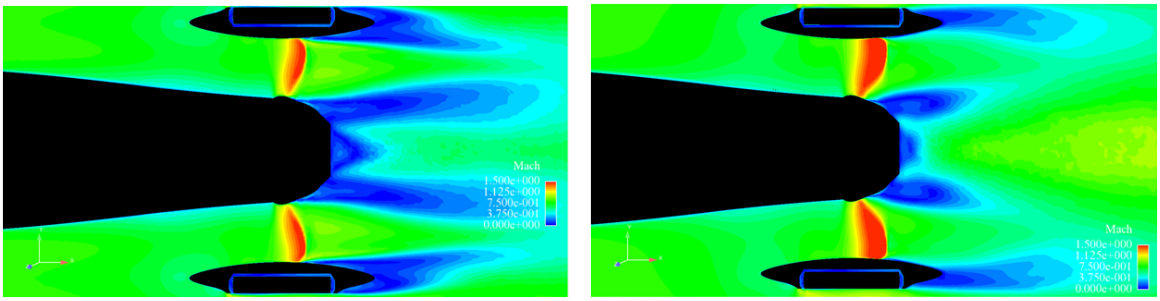

(a) Spalart-Allmaras - JST (b) Spalart-Allmaras - HLLC

Figure 15: Iso-contour of Mach numbers at $M_\infty = 0.85$ and height = 0.5m.

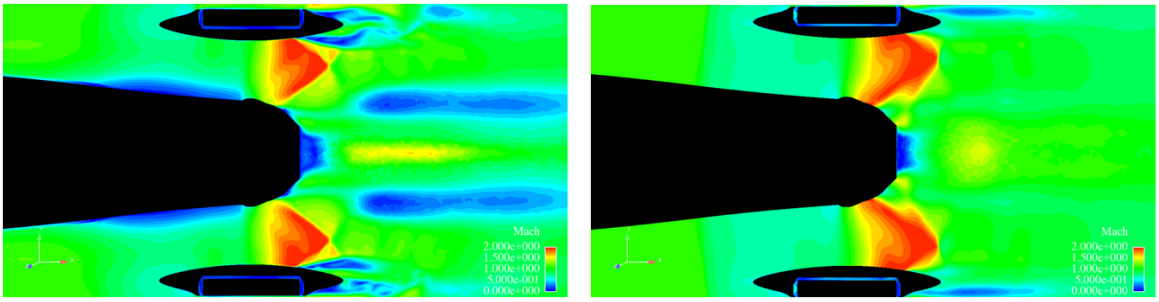

(a) Spalart-Allmaras - JST (b) Spalart-Allmaras - HLLC

Figure 16: Iso-contour of Mach numbers at $M_\infty = 1.1$ and height = 0.5m.

5 CONCLUSIONS

An assessment of three popular turbulent models is performed in 3-D aerodynamic cases. The FLITE flow solver by utilizing the Spalart–Allmaras, the Wilcox $k-\omega$ and the Menter SST turbulence models has been applied in a supersonic flat plate, RAE2822 airfoil, the ONERA M6 wing and the supersonic car BLOODHOUND SSC.
The transonic RAE2822 airfoil possesses a strong shock-boundary layer interaction with an induced separation. The ONERA M6 wing exhibits a very complex flow phenomena such as double shocks, high-lift flow, strong adverse pressure gradients and streamline curvature effects. For attached flows or middle separated flows, there is not a clear superiority of the two-equation turbulence models over the one-equation Spalart–Allmaras model. However, the ONERA M6 wing at an angle of attack equal to $\alpha = 6.0^o$, where flow separation is dominant, has indicated the contrary. The Menter SST has shown the best compromise between accurately describing the physics of the flow and numerical stability. The shear stress transport (SST) formulation may be the reason for this.
Numerical predictions over a supersonic car, the "BLOODHOUND SSC" [1], have also been carried out and some preliminary results have been shown for the Spalart–Allmaras and the Wilcox $k-\omega$ turbulence models together with the JST and HLLC convective flux schemes. Interestingly, the type of convective flux computation is more influential than the turbulence model itself in the aerodynamic forces over the car. Furthermore, important insights were acquired on flow phenomena. Future investigation will focus on unsteady flow simulations over the supersonic car. This could be more appropriate in realistically capturing the complex turbulent structures governed by shock-boundary layer interactions and highly-separated flows.

REFERENCES

[1] http://www.bloodhoundssc.swan.ac.uk/

[2] P.R. Spalart, S.R. Allmaras, A one equation turbulence model for aerodynamics flows, *30th Aerospace Science Meeting and Exhibit*, Reno, USA. AIAA paper 92-0439 (1992).

[3] D.C.Wilcox, Turbulence Modeling for CFD, DWC Industries, Inc. La Canada, California (2006).

[4] F.R. Menter, Review of the shear-stress transport turbulence model experience from an industrial perspective, *Int. J. of Computational Fluid Dynamics* **23** 4 pp 305-316 (2009).

[5] K. Morgan, J. Peraire, J. Peiro and O. Hassan, The computation of 3-dimensional flows using unstructured grids, *Computer Methods in Applied Mechanics and Engineering*, **87** Issue: 2-3 pp 335-352 (1991).

[6] S.B. Pope, TURBULENT FLOWS, *Cambridge University Press* August 2000.

[7] P. Moin and K. Mahesh, DIRECT NUMERICAL SIMULATION: A Tool in Turbulence Research, *Annual Review of Fluid Mechanics*, **30** pp 539-578 (1998).

[8] C. Meneveau and J. Katz, Scale-invariance and turbulence models for large-eddy simulation, *Annual Review of Fluid Mechanics* **32** pp 1-32 (2000).

[9] J. Frohlich and D. von Terzi, Hybrid LES/RANS methods for the simulation of turbulent flows, *Progress in Aeropace Sciences* **44** Issue: 5 pp 349-377 (2008).

[10] P. Catalano and M. Amato, An evaluation of RANS turbulence modelling for aerodynamic applications, *Aerospace Science and Technology*, **7**, Issue 7 pp 493-509 (2003).

[11] K.A. Sørensen, A multigrid accelerated procedure for the solution of compressible fluid flows on unstructured hybrid meshes. PhD thesis, University of Wales, Swansea, (2002).

[12] F.M. White, Viscous Fluid Flow, McGraw Hill (1974)

[13] H. Schlichting, Boundary Layer Theory, McGraw-Hill, New York (1968).

[14] P. Cook, M. McDonald, M. Firmin, Aerofoil RAE2822pressure distributions and boundary layer and wake measurements, Report AR138, AGARD, Paris (1979).

[15] V. Schmitt and F. Charpin, Pressure distributions of the ONERA M6 wing at transonic Mach numbers, Report AR138, AGARD, Paris (1979).

[16] A. Jameson, W. Schmidt and E. Turkel, Numerical simulation of the Euler equations by finite volume methods using Runge-Kutta time stepping-schemes. AIAA Paper 81-1259 (1981).

[17] A. Harten, P. D. Lax, and B. van Leer, On upstreaming differencing and Godunov-type schemes for hyperbolic conservation laws, SIAM Rev., 25, 35 (1983).